



## PAPER

## Quantum resonant optical bistability with a narrow atomic transition: bistability phase diagram in the bad cavity regime

## OPEN ACCESS

## RECEIVED

24 May 2023

## REVISED

31 August 2023

## ACCEPTED FOR PUBLICATION



13 September 2023

## PUBLISHED

29 September 2023

Original Content from  
this work may be used  
under the terms of the  
[Creative Commons  
Attribution 4.0 licence](#).

Any further distribution  
of this work must  
maintain attribution to  
the author(s) and the title  
of the work, journal  
citation and DOI.

D Rivero<sup>1,2</sup>, C A Pessoa Jr<sup>1</sup>, G H de França<sup>1</sup>, R C Teixeira<sup>3</sup> , S Slama<sup>4</sup>  and Ph W Courteille<sup>1,\*</sup><sup>1</sup> Instituto de Física de São Carlos, Universidade de São Paulo, São Carlos, SP 13566-970, Brazil<sup>2</sup> Institute for Quantum Electronics, ETH Zürich, 8093 Zürich, Switzerland<sup>3</sup> Departamento de Física, Universidade Federal de São Carlos, São Carlos, SP 13565-905, Brazil<sup>4</sup> Center for Quantum Science and Physikalisches Institut, Eberhard-Karls Universität Tübingen, Auf der Morgenstelle 14, 72076 Tübingen, Germany

\* Author to whom any correspondence should be addressed.

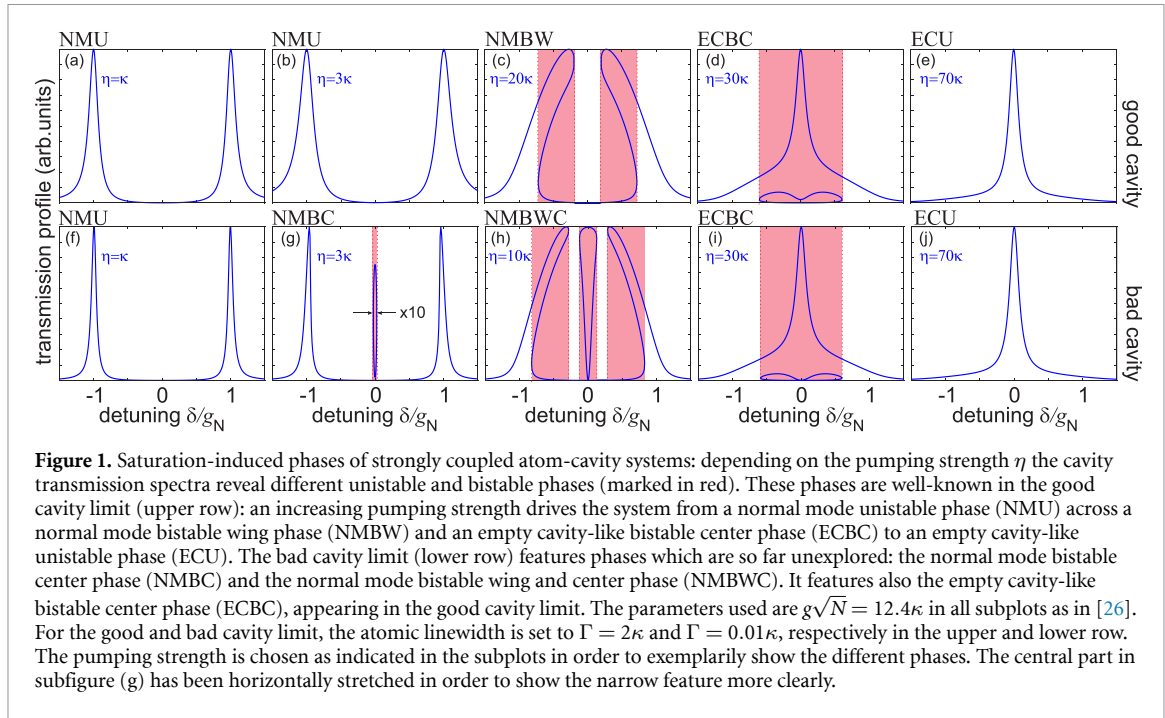
E-mail: [philippe.courteille@ifsc.usp.br](mailto:philippe.courteille@ifsc.usp.br)**Keywords:** ring cavity, resonant bistability, ultracold atoms, normal mode splitting

## Abstract

We report on the observation of a novel manifestation of saturation-induced optical bistability in a resonantly pumped optical ring cavity interacting strongly with a cloud of atoms via a narrow atomic transition. The bistability emerges, above a critical pump rate, as an additional peak in the cavity's normal mode spectrum close to atomic resonance. This third transmission peak is usually suppressed due to strong resonant absorption, but in our experiment it is visible because of the linewidth of the atomic transition being much smaller than that of the cavity, which sets the experiment into the bad-cavity regime. Relying on complete saturation of the transition, this bistability has a quantum origin and cannot be mimicked by a classical material presenting a nonlinear refraction index. The appearance of the central peak in addition to the normal modes is predicted by a semi-classical model derived from the Tavis–Cummings Hamiltonian from which we derive a bistability phase diagram that connects our observations with former work on optical bistability in the good cavity regime. The phase diagram reveals several so far unexplored bistable phases.

Cavity-mediated interactions between atoms provide a promising route to generate non-trivial interatomic correlations leading to phenomena such as spin-squeezing [1–9], superradiant lasing [10–17], or quantum state magnification [18, 19], which are of utmost interest for metrological applications. One important request is that the rate of spontaneous emission  $\Gamma$  is small, leaving cavity decay occurring at a rate  $\kappa$  as the only available decay channel. In this limit, known as the ‘bad cavity’ regime, non-classical features in the photon statistics become more robust [20–24] and quantum correlations more stable. A second requirement is a high collective cooperativity, which is a necessary condition for light emitted from one atom to be reabsorbed by another one and thus information to be shared between atoms. These ingredients can lead to nonlinear system dynamics and eventually to bistability. For the optical mode the bistability can manifest as two stable states of transmission, whose realization depend on the history of the system. The bistability can originate in different features of the system. For example in [25–29], it is caused by saturation, in [30, 31] by optomechanical coupling, and in [32–34] by the multilevel structure of the ground state. Although all those features are ultimately linked to atomic properties, not all of them can be considered as ‘quantum’, as some can be mimicked, for example, by the nonlinear classical refraction index of a crystal. Resonant regions of parameters are most likely to hold a bistable regime associated with quantum correlations: the resonance condition ensures high saturation and therefore strong nonlinearity caused by the quantized nature of the transition.

Strong interaction between the atoms and the cavity mode leads to normal mode splitting of the cavity's transmission resonance when the frequency of the atomic transition is close to the resonance of the empty cavity [35–39]. From a semi-classical model of light-atom interaction, the atom-cavity resonances can be found at those frequencies where the acquired phase for a round trip of the light inside the cavity filled with



atoms is zero [27, 35]. For high collective cooperativity and moderate intracavity intensities, this zero-phase condition generates three resonances: two that correspond to the normal mode splitting plus a central one that is, in practice, heavily suppressed due to atomic absorption. But the use of a narrow atomic transition can change this scenario and open a saturation-induced transparency window, allowing for an observation of this central resonance.

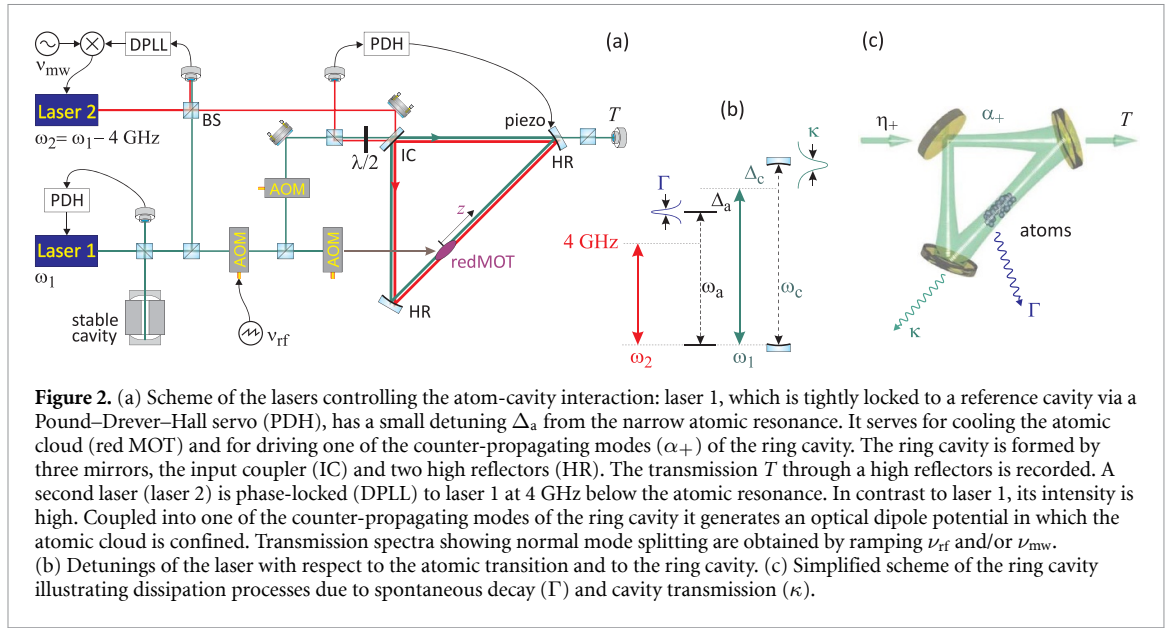
In this work, contrasting with experiments [20, 25, 26, 28] carried out in the good-cavity limit, we choose the narrow intercombination transition  $^1S_0 \leftrightarrow ^3P_1$  in atomic strontium with a decay rate  $\Gamma/2\pi = 7.5$  kHz for interaction with a cavity mode with amplitude decay width  $\kappa/2\pi = 3.4$  MHz. This sets the system deep into the bad cavity limit. At the same time the atom-field coupling strength  $g_N = g\sqrt{N}$  with coupling constant  $g/2\pi = 9.1$  kHz is collectively enhanced by a number of up to  $N = 200\,000$  atoms such that the atoms are strongly coupled to the cavity. This allows us to probe the normal modes in the bad cavity limit featuring a series of bistable phases, which are different from the ones in the good cavity limit. Figure 1 shows normal mode spectra calculated for different cavity pump rates  $\eta$ . In particular, we can excite and study the resonant normal mode, which is suppressed in the good cavity limit [26]. In figure 1 this is seen by comparing the spectra (c) and (h). Note that the used transition has a low enough saturation intensity to be saturated with even single photons in our cavity.

In section 1 we present our experimental setup, procedure, and measurements. In section 2 we expose our model derived from the many-atom Dicke Hamiltonian. The stationary intracavity photon number predicted by the model allows us to calculate the normal modes under special consideration of the respective roles of atomic bunching, particular pumping schemes of the ring cavity modes, and saturation of the atomic transition. We verified that our theoretical model describes the instabilities observed in other experiments [27, 28]. The measurements are quantitatively compared with our model and interpreted in section 3.

## 1. Experiment

### 1.1. Experimental setup

The experimental setup has been presented in detail in [40]. In short, a cloud of about  $N = 200\,000$   $^{88}\text{Sr}$  atoms is cooled to temperatures around  $1\,\mu\text{K}$  and transferred into the mode volume of a ring cavity operated near the narrow intercombination line with the transition wavelength  $\lambda_a = 689$  nm connecting the energy levels  $(5s)^2\,^1S_0$  and  $(5s5p)\,^3P_1$ . The atomic cloud is confined to the mode volume by the optical dipole potential formed by laser beams coupled into a  $\text{TEM}_{00}$  mode of the ring cavity (laser 2 in figure 2) under  $p$ -polarization, where the finesse of the cavity is low ( $F \approx 100$ ). The length of the ring cavity is stabilized to this laser 2 via a Pound–Drever–Hall servo electronics. Laser 2, which is tuned  $\Delta_{\text{dip}}/2\pi \approx -530\Gamma$  to the red of the strontium resonance is, in turn, locked via a digital phase-locked loop (DPLL) to a second laser (laser 1 in figure 2), which itself is stabilized to a stable supercavity and operated near the strontium resonance.



Laser 1 serves for the last cooling stage of the atomic cloud, and also as a probe for the atom-cavity interaction. In this latter role, the light of laser 1 is passed through AOMs, driven by a tunable radio-frequency  $\nu_{rf}$  and permitting to ramp the laser frequency  $\omega$  with respect to the atomic resonance  $\omega_a$ , thus generating a controlled detuning  $\Delta_a = \omega - \omega_a$ , and with respect to the ring cavity resonance  $\omega_c$ , generating a detuning  $\Delta_c = \omega - \omega_c$ . On the other hand, we can control the detuning between the cavity and the atomic resonance,  $\Delta_{ca} = \omega_c - \omega_a = \Delta_a - \Delta_c$ , via the microwave-frequency  $\nu_{mw}$  of the DPLL [40].

Injected into one of the two counter-propagating modes of the ring cavity, laser 2 generates an optical dipole trap, in which the atomic cloud adopts a smooth density distribution elongated along the cavity's optical axis. Part of the light power of laser 1 is coupled as probe light into a TEM<sub>00</sub> mode of the ring cavity using s-polarization, where the finesse of the cavity is high ( $F \approx 1200$ ), counter-propagating with laser 2. The probe light transmitted through the pumped mode through a high reflecting mirror (transmission  $T_{hr} \approx 0.001$ ) is filtered by a polarizing beamsplitter, coupled into optical fibers and monitored. We infer the intracavity power  $P$  from the transmitted probe light power  $P_{hr} = T_{hr}P = T_{hr}\hbar\omega\delta_{fsr}n$ , where  $\delta_{fsr} = 8.23$  GHz is the free spectral range of the ring cavity and  $n$  the intracavity photon number. Subscripts  $\pm$  refer to counter-propagating modes of the ring cavity. In the following we assume that only the mode denoted by  $\alpha_+$ , where  $|\alpha_+|^2 = n$ , is pumped and that the mode  $\alpha_-$  is filled only via photonic backscattering by the atomic cloud.

The cavity pump rate  $\eta_+$  is an experimental parameter which can be determined from the photon number in the empty cavity under resonant driving,  $\eta_+/\kappa \equiv \alpha_+(N=0, \Delta_c=0)$ . It allows to express the ring cavity transmission as,  $T = |\alpha_+/\alpha_\eta|^2$ . With the saturation parameter given by  $s \equiv 2\Omega^2/\Gamma^2$  defined via the Rabi frequency  $\Omega \equiv 2g|\alpha_+|$  we find that the transition is saturated by a mean photon number of  $|\alpha_{sat}|^2 \approx 0.087$  corresponding to a power of  $P_{sat} = \hbar\omega\delta_{fsr}|\alpha_{sat}|^2 \approx 0.2$  nW. In practice, we typically use saturation parameters in the range  $s = P/P_{sat} \approx 100 \dots 1000$ . The single-photon saturation  $s_1$  and the single-atom cooperativity  $\Upsilon$  are important parameters characterizing our coupled atom-cavity system,

$$s_1 \equiv \frac{8g^2}{\Gamma^2} \approx 11.5 \quad , \quad \Upsilon \equiv \frac{4g^2}{\kappa\Gamma} \approx 0.013 \quad . \quad (1)$$

## 1.2. Measurements

We record normal mode spectra by scanning  $\Delta_a$  for fixed  $\Delta_{ca}$ . The typical duration of a scan is  $\Delta t_{scan} = 0.25$  ms. Repeating the scan for various  $\Delta_{ca}$  we obtain the two-dimensional spectra shown in figures 3(a)–(c) with false-color coding. Yellow indicates maximum cavity transmission and blue an impermeable cavity reflecting the pump light completely.

The figures 3(a)–(c) show transmission spectra measured for different pump rates  $\eta_+$ . The spectra show a number of interesting features: (i) The normal modes are clearly visible as two resonances describing an avoided crossing. These resonances are emphasized by dashed black lines in the figures. (ii) Near the atomic resonance, around  $\Delta_a \simeq 0$ , the spectra develop a narrow ridge of high transmission bridging the normal modes. Normal mode spectra recorded by scanning  $\Delta_a$  near the atom-cavity resonance, i.e. around  $\Delta_{ca} \simeq 0$ , therefore exhibit three peaks instead of two. (iii) The ridge is flanked by discontinuous steep precipices into

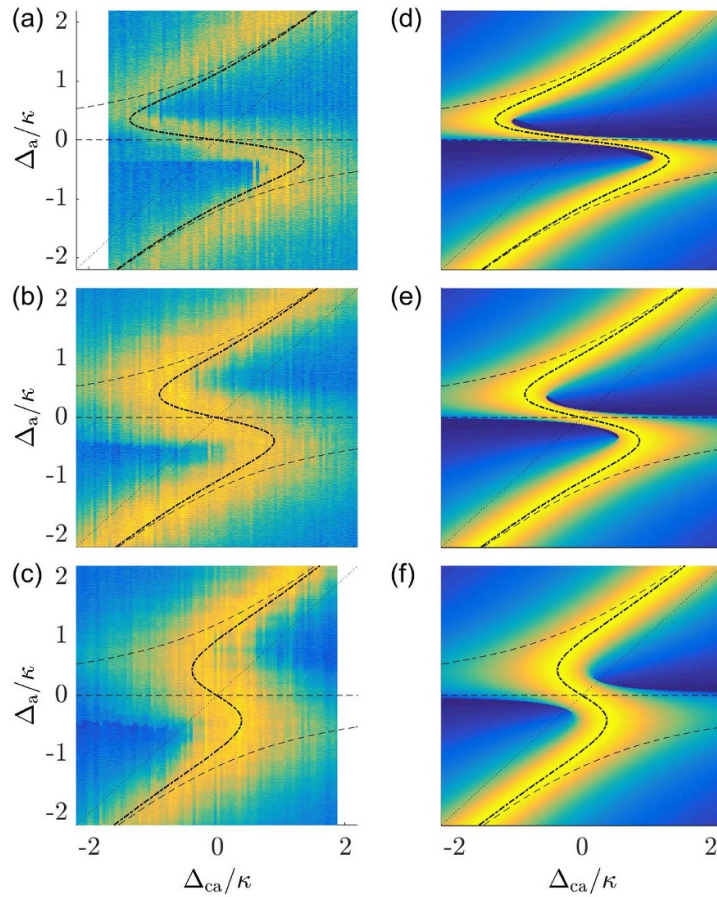


**Figure 3.** (a)–(c) Measured cavity transmission for various  $\eta_+$  taken with  $N = 200\,000$  atoms: The pump rate is varied from (a)  $\eta_+ = 110\kappa$  over (b)  $140\kappa$  to (c)  $200\kappa$ . (d)–(f) Calculated transmission spectra using equation (3) for pump rates corresponding to those of (a)–(c) and all other experimental parameters as specified in the text. For the spectral regions presenting bistability, the solution shown is the one with highest transmission. The diagonal black dotted lines show the mode of an empty cavity ( $N = 0$ ). The black dash-dotted lines are calculated from equation (4) using a saturation broadening estimated from  $\Omega_\eta = 2g\eta_+/\kappa$ . The dashed lines correspond to setting  $\Omega_\eta = 0$ .

dark regions appearing as sharp horizontal features in the false color plots. The additional central peak has sharp edges, pointing to bistable behavior of the cavity transmission.

Comparing different spectra taken for different pump rates  $\eta_+$  we notice additional features: (iv) The (vertical) width of the bridge between the normal modes in figures 3(a)–(c), that is, the width of the central peak in  $\Delta_a$ -scans, increases with stronger pump rates  $\eta_+$ . (v) As the pump rate is increased, the discontinuous ledges are ‘pushed’ away from resonance towards higher  $|\Delta_{ca}|$ . At sufficiently strong pumping the avoided crossing of the normal modes turns into a dispersive lineshape.  $\Delta_a$ -scans near atom-cavity resonance still show three peaks, but do not any longer exhibit discontinuities arising from bistable behavior.

Figure 4 shows a more detailed study of the dependence of the normal mode spectra on the pump rate  $\eta_+$ . In figure 4(a) the pump laser was scanned from  $\Delta_a = -2.2\kappa$  to  $+2.2\kappa$ , immediately followed by a scan in the inverse direction exhibited in (b). The features to be extracted from these measurements are:

(vi) There is a central peak around  $\Delta_a = 0$  bordered by sharp edges. The central peak corresponds to the ‘bridge’ of figures 3(a)–(c). (vii) We note a hysteretic behavior of the sharp edges, as the position of the central peak in figure 4(b) is slightly shifted as compared to (a). The latter feature is seen more clearly in a single scan taken at a pump rate of  $\eta_+ = 120$  [white dashed lines in figures 4(a) and (b)] and plotted in figure 4(d). (viii) The central peak increases its width at high pump rates. (ix) The distance between the normal mode peaks diminishes when increasing the pump rate very far beyond saturation. Eventually all peaks merge into a single one.

We identify in all those features a bistability mechanism of a different kind than previously reported in the literature for atom-cavity systems. In the next sections we develop a semiclassical theory that fits well our data and grasps this new mechanism [41].

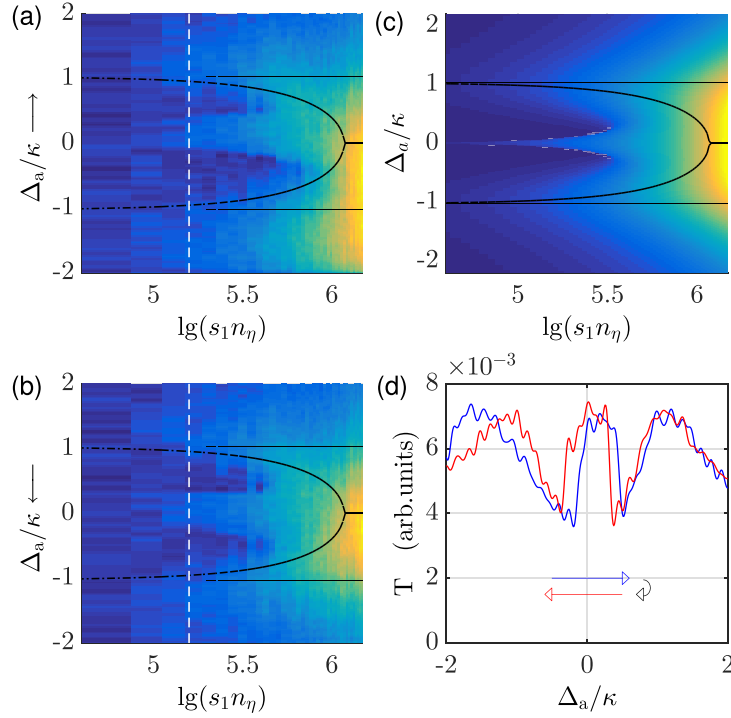


**Figure 4.** Pump rate dependence of the normal mode spectrum: (a) resp. (b) show normal mode spectra taken on resonance ( $\Delta_{ca} = 0$ ) as a function of pump laser power,  $s_\eta = s_1 n_\eta = s_1 \eta_+^2 / \kappa^2$ , for the atom-cavity detuning scanned in real time from lower to higher (resp. higher to lower) values. Above saturation the distance between the normal modes diminishes with increasing pump power. (c) Simulation based on the same equations as for figure 3 using the same experimental parameters as for curves (a) and (b). The dashed lines show the low saturation value of the normal mode splitting. The dash-dotted lines denote the frequencies of the normal modes calculated from equation (4). The measurements also show a hysteresis-like behavior. Looking at vertical cuts along the white dashed line traced in figures (a) and (b) one observes that the jump between opaque and transparent solutions is always delayed in the scanned direction (blue and red curves in figure (d), the arrows indicate the scan direction). Note that the scan back sees the second normal mode (left peak of red curve) at reduced atomic distance. We attribute this to heating or trap loss during the scan causing a reduction of the normal mode splitting.

## 2. Theoretical description

The energy spectrum of the coupled Tavis-Cummings system consisting of  $N$  atoms and one cavity mode has been calculated in [42, 43]. In the following we will restrict to calculating the transmission spectra  $T(\Delta_{ca}, \Delta_a)$  for our ring cavity [44].

The relevant degrees of freedom of our system are the counter-propagating field modes of the ring cavity, described by the field operators  $\hat{a}_\pm$ , and the excitation of atoms located at positions  $z_j$  along the cavity's optical axis, denoted by the Pauli operators  $\hat{\sigma}_j^\pm$  and  $\hat{\sigma}_j^z$ . To obtain an expression describing normal mode splitting of our coupled atom-ring cavity system (see appendix A.1) we write down the collective Hamiltonian and derive Heisenberg equations for the degrees of freedom. Spontaneous emission and cavity decay are accounted for by jump operators for the dissipative processes occurring at rates  $\Gamma$ , respectively,  $\kappa$ . Neglecting all quantum correlations we perform a semiclassical decorrelation [26] and derive the steady-state solution for the expectation values  $\alpha_\pm = \langle \hat{a}_\pm \rangle$ . It reads (see equation (22) of the appendix),

$$\sum_{j=1}^N \frac{U_\gamma (\alpha_\pm + e^{\mp 2i k z_j}) \alpha_\mp}{1 + 2|U_\gamma/g|^2 |e^{i k z_j} \alpha_+ + e^{-i k z_j} \alpha_-|^2} = \eta_\pm - \Delta_\kappa \alpha_\pm. \quad (2)$$

with the abbreviations,  $U_\gamma \equiv U_0 - \nu \gamma_0 \equiv g^2 / (\Delta_a + i \frac{\Gamma}{2})$  and  $\Delta_\kappa \equiv \Delta_c + i \kappa$ .

The expression (2) cannot be solved analytically except in some particular limits. The first simplification consists in assuming that the cavity is pumped from one side only,  $\eta_- = 0$ , and that the cloud is homogeneously distributed over the mode volume of the cavity. In that case, we may neglect backscattered light altogether,  $\alpha_- = 0$ , and equation (2) simplifies to,

$$\alpha_+ = \frac{\eta_+}{\Delta_\kappa - \frac{N U_\gamma}{1 + 2|U_\gamma \alpha_+ / g|^2}}. \quad (3)$$

We note that this expression coincides with the equation (10) used by Gripp *et al* [26].



Taking the modulus squared of this expression, we arrive to a cubic equation for the average number of photons inside the cavity mode  $n = |\alpha_+|^2$  [equation (25) of the [appendix](#)], which presents more than one stable solution for a certain range of parameters. This bistable behavior leaves an experimental signature in the form of sudden jumps of the cavity transmission upon changing certain parameters, e.g. the pump light intensity or detuning, as already mentioned in the discussion of figures 3(a)–(c) in section 1.2. The theoretical transmission spectra exhibited in figures 3(d)–(f) are proportional to the intracavity photon number  $n$  and calculated for the same experimental parameters as figures 3(a)–(c), respectively. For the bistable parameter regions, where more than one stable solution exists, the solution with highest transmission is shown.

### 2.1. On-resonance and off-resonance bistability

The condition of zero phase shift for the intracavity light field  $\alpha_+$  with respect to the pump field  $\eta_+$  can be found by setting the imaginary part of the right-hand side of equation (3) to zero. It yields,

$$\Delta_{ca} = \Delta_a - \frac{Ng^2\Delta_a}{\Delta_a^2 + \Gamma^2/4 + \Omega_\eta^2/2}. \quad (4)$$

In this expression  $\Omega_\eta = 2g\eta_+/\kappa$  is the maximum Rabi frequency, i.e. the Rabi frequency if all impinging photons would enter the cavity. The corresponding curve is shown in figure 3 as dash-dotted lines. We also show in dashed lines the corresponding zero-phase shift curve for vanishing pump field,  $\Omega_\eta \rightarrow 0$ . We note that it follows closely the maxima of the experimental transmission curves for all range of experimental parameters. Although this condition is generic for most experiments dealing with cavities filled with atoms and operated in the strong collective coupling regime, the central peak is commonly suppressed due to strong resonant absorption of the light by the atoms. In our case, the width of the atomic transition is very small, and we can expect that very little light intensity will already saturate the transition, thus changing this scenario. The rate of photon injection into the cavity,  $\eta_+ = \kappa n_\eta$ , that saturates all atoms roughly equalizes the rate at which they emit photons once they are saturated,  $N\Gamma/2$ . This means that for  $n_\eta \gtrsim N\Gamma/2\kappa$ , the atoms become transparent, and a transmission window opens around the empty cavity resonance. This quantum nonlinear feature of the cavity transmission entails the appearance of a bistable spectral region near resonance. The calculations in the [appendix](#) [see (46)] indeed show that for  $\Delta_a = \Delta_c = 0$  a lower bound on the pump rate for the appearance of two stable solutions (the signature of a bistable behavior) is,

$$n_\eta \gtrsim \frac{N\Gamma(1 + \sqrt{3}/2)}{2\kappa}, \quad (5)$$

and the width of the bistable region for  $\Delta_c = 0$  is given by equation (52) as,

$$|\Delta_a| \simeq \frac{g}{\sqrt{2}} \sqrt{n_\eta - \frac{N\Gamma}{2\kappa}} = \frac{1}{2} \sqrt{\frac{\Omega_\eta^2}{2} - \frac{\Gamma^2\Upsilon_N}{4}}. \quad (6)$$

We will call this bistability mechanism *on-resonance bistability*. It is present for example in the NMBC phase shown in figure 1(g).

Gripp *et al* [26] find a qualitatively different modification of the normal mode splitting when the intensity is increased, reproduced here in figures 1(a)–(e). For their parameters, the bistability emerges off-resonance, at the inner edge of each of the normal mode splitting peaks. It appears for example in the NMBW phase shown in figure 1(c). The underlying mechanism follows a prototypical intensity-driven bistability also found in anharmonic classical mechanical oscillators [45] subject to an intensity-dependent frequency shift of the normal mode splitting resonances. Upon further increase of the pump intensity, this bistability mechanism eventually leads to a merger of the two normal mode peaks into a single transmission peak. For  $\kappa, \Gamma \ll g\sqrt{N}$  (i.e. for a normal mode splitting much larger than the width of the normal mode resonances), this happens when the two local extremes of the zero-phase condition curve  $\Delta_{ca}$  as a function of  $\Delta_a$  as given by equation (4) merge into a single point ( $d\Delta_{ca}/d\Delta_a|_{\Delta_a=0} = 0$ ). This is the case when

$$Ng^2 = \Gamma^2/4 + \Omega_\eta^2/2. \quad (7)$$

We may reasonably expect that, in order to have on-resonance bistability, the critical intensity for its appearance, as described by equation (5), must be smaller than the critical intensity for the merging of the off-resonance bistable spectral intervals. For  $Ng^2 \gg \Gamma^2/4$ , this amounts to  $\Gamma(1 + \sqrt{3}/2) \lesssim \kappa$ , which is qualitatively the condition for the bad-cavity regime. Thus, it is the narrowness of the strontium transition that allows us to observe the new bistable mechanism in our experiment. This new mechanism for bistability relies not only on the nonlinearity of the atom-cavity interaction, but also on the complete saturation of the

atomic population to cause full transparency of the cavity to light. Thus, it cannot be generated by a simple nonlinear susceptibility.

## 2.2. Comparison to experiment

The calculated spectra in figures 3 and 4 are in good qualitative agreement with the measured ones. For instance, comparing the spectra of figures 4(a) and (b) we notice that the bistability around the central peak is symmetrically inverted when the scan direction is also inverted, and that the maximum of the transmission is roughly independent of the pump rate, showing no anharmonicity in the resonance frequency. Those features are also evident in the theoretical spectra of figures 1(f)–(j).

On the other hand, while the observed spectral width of the normal mode resonances agrees well with the simulations and does not depend on the pump rate, the spectral width of the bistable region is systematically larger than predicted by simulations. As illustrated in figure 4(c), the width of the bistable region should be dominated by power broadening. But from earlier work [26, 28, 29, 32] we know that the onset of bistability is accompanied by oscillations and hysteresis, that can lead to deformations and broadening of the spectra not grasped by our *stationary model*.

As mentioned in section 1.2, we indeed observe hysteresis behavior. The oscillations are manifestations of a ringing induced by a time lag between the evolution imposed by the scan and the evolution of the degrees of freedom characterizing the system, which becomes relevant when the slowest time constant of our system, which is the atomic decay rate  $2\pi/\Gamma = 0.13$  ms, is comparable to or slower than the scan duration  $\Delta t_{\text{scan}} = 0.25$  ms. We indeed observe deformation of the spectra when shorter scan times  $\Delta t_{\text{scan}}$  are chosen. However, our photodetector, being optimized for high sensitivity to weak light intensities, is too slow to resolve the fast oscillations.

An example for a spectral deformation can be observed in figure 4(d), where the normal mode splitting is found to be larger on the first scan from negative to positive detunings (blue curve) than on the subsequent scan in backward direction (red curve). The deformations of the spectra become stronger when *longer* scan times are used. A possible reason can be heating of the atomic cloud during the scan causing a reduction of the effective number of atoms interacting with the cavity.

We also note that, in sufficiently strong magnetic fields, a phenomenon called magnetically induced transparency (MIT) [46] induced by the Zeeman substructure of the excited  $^3P_1$  state can add a central feature to the normal mode spectra even at very low saturation. Numerical simulations performed with linearized equations of motion, however, show a qualitatively different behavior as the one observed in figure 3. Furthermore, we tested applying different magnetic fields without noticing a dependency.

## 3. Discussion

At vanishing pump rate, the shape of the transmission spectrum of the cavity strongly interacting with the atomic cloud becomes independent on the single-photon saturation parameter  $s_1$  (see equation (25) in the [appendix](#)). In particular, for collective strong coupling,  $g\sqrt{N} > \kappa, \Gamma$ , the spectrum presents a splitting of the resonance reminiscent of two strongly coupled harmonic oscillators.

For collective strong coupling and a non-vanishing pump rate, the nonlinearity of the atom-light interaction changes this simple scenario. Two other parameters then together determine whether the system will be bistable or not and in which frequency interval bistability will occur. The first parameter is, obviously, the pump rate  $\eta_+$  which can be represented either by the average photon number  $n_\eta$  that it generates inside the cavity at its bare resonance, or by the saturation parameter  $s_\eta = s_1 n_\eta$ .

Another crucial parameter for the emergence of bistability is the ratio between spontaneous and cavity decay width,  $\Gamma/\kappa$ , which is the parameter that distinguishes between the good and bad cavity regime. In figure 5 we calculate the transmission profile as a function of  $\Delta_a$  and  $\eta_+$  obtained from the analytical solution of equation (3). In figures 5(b) and (d) the atomic decay width and the atom-cavity coupling strength were chosen as those of our experiment,  $\Gamma = 0.0022\kappa$  and  $g_N = 1.2\kappa$ . The emergence of on-resonance bistability is clearly visible in a wide range of pump rates. On the other hand, the spectra exhibited in figures 5(a) and (c) were calculated for a much stronger spontaneous decay rate  $\Gamma = 2\kappa$  and  $g_N = 12.4\kappa$ , corresponding to the parameters used by Gripp *et al* [26], and show a bistable behavior that emerges from the deformation of the normal mode peaks, until they merge to a single peak for high enough saturation.

### 3.1. Bistability phase diagram

In order to derive the complete phase diagram we have solved the steady-state equations for the transmission spectrum for various values of the atomic transverse decay rate  $\Gamma/2$  and the pump rate  $\eta_+$ , both scaled to the cavity linewidth  $\kappa$ . Some examples have already been plotted in figure 1. Details on how we solve the equations are given in the [appendix A.2](#).

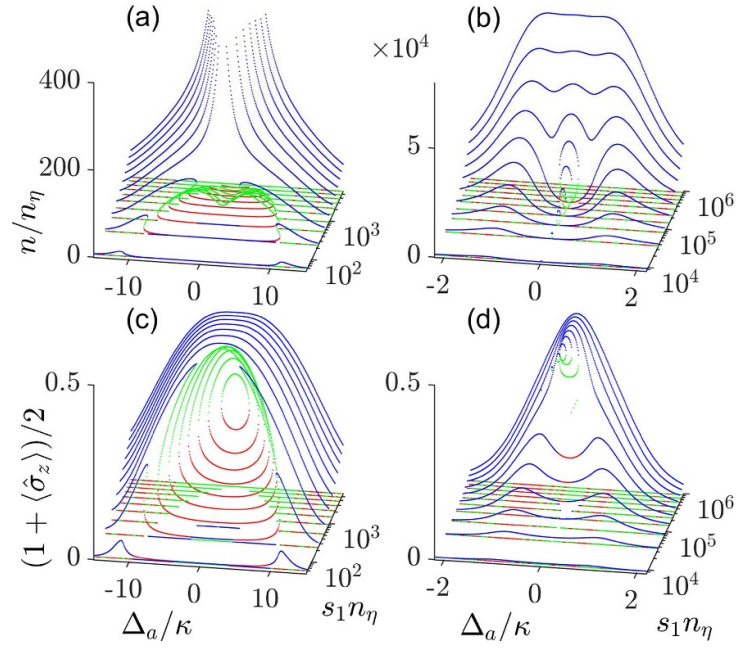


**Figure 5.** (a), (b) Transmission profiles as a function of  $\Delta_a$  and  $\eta_+$  obtained from the analytical solution of equation (3). The atomic decay width and the collective atom-cavity coupling strength were chosen for (a)  $\Gamma = 2\kappa$  and  $g_N = 12.4\kappa$  and for (b)  $\Gamma = 0.0022\kappa$  and  $g_N = 1.2\kappa$ . Different colors are used to highlight different solutions in the bistable regime. (c), (d) Spectra of the excited state populations corresponding to (a), (b) calculated from the expression (32) in the appendix.

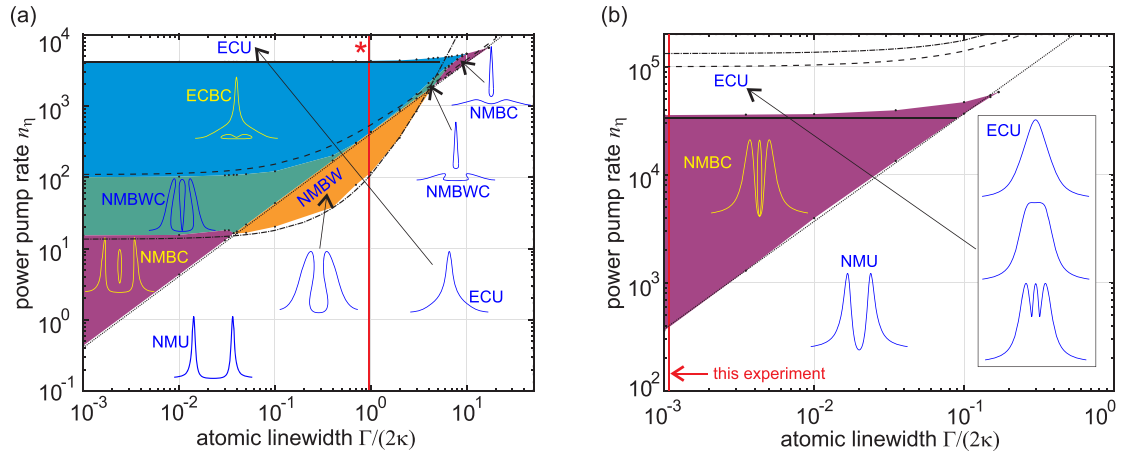
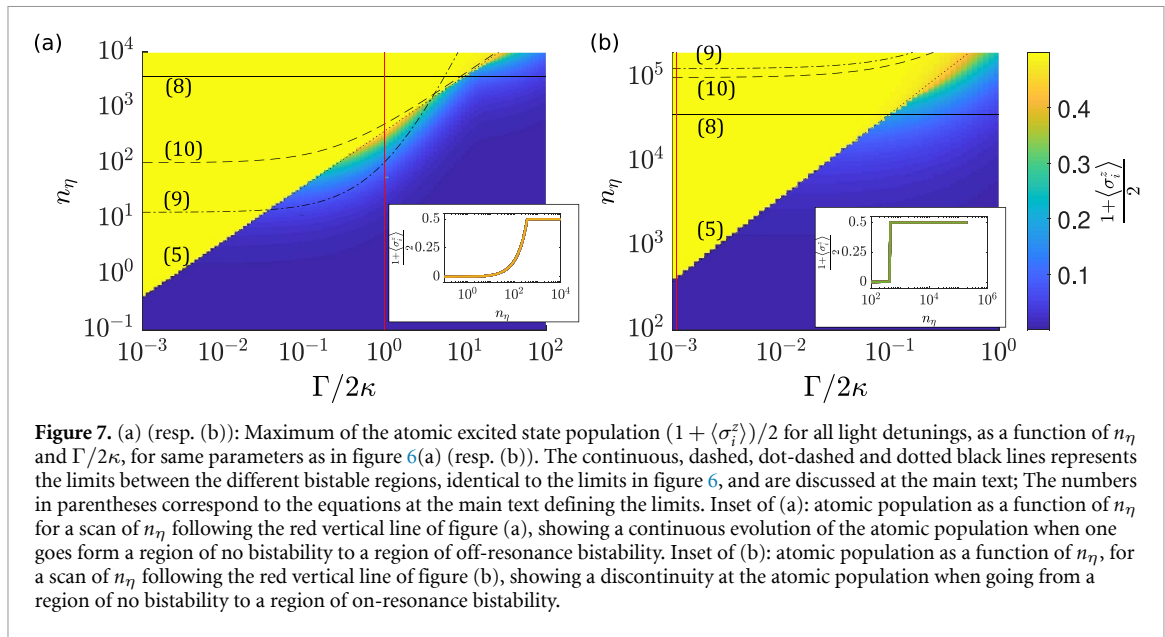


**Figure 6.** Simulated phase diagram of the coupled atom-cavity system with saturation for (a) collective coupling strength  $g_N = 12.4\kappa$  as in [26] (marked by \*) and (b)  $g_N = 1.2\kappa$  as in our experiment. Observation of the NMBC phase is featured within the bad cavity limit, while the NMBW and NMBC phases disappears in the bad cavity limit. The black lines separating the different phases are given by analytical formulas. The dotted diagonal line marks the onset of on-resonance bistability, and the dash-dotted line that at the wings. The dashed line indicates the merging of bistability at the wings and at the center, and finally the solid line marks the maximum pump rate to show bistability. Note that NMBWC- and NMBC-like phases exist also in the strongly coupled good cavity limit, i.e. for  $\kappa < \Gamma/2 < g_N$ . In the case of weak coupling reached for even larger atomic linewidth no bistable phase exists. The phase diagram (b) containing the experimental situation is much simpler because of the weaker coupling strength  $g_N = 1.2\kappa$ . Here, only the NMBC bistable phase survives.

We classify the bistable solutions by the overall shape of the spectrum, i.e. resembling either a normal mode or an empty cavity spectrum, and by the frequencies at which the bistability occurs, i.e. either in the wings or in the center of the spectrum. In figures 6(a) and (b) we compiled phase diagrams for two different situations: figure 6(a) is done for  $g_N = 12.4\kappa$ , reproducing the situation of Gripp *et al* [26], while figure 6(b) is obtained for the collective coupling constant  $g_N$  of our experimental system.

The parameter region for the occurrence of on-resonance bistability, identified by the existence of three positive real solutions for  $\Delta_a = \Delta_c = 0$ , is limited to large values of  $n_\eta$  by the condition (5). In contrast, when the collective cooperativity is larger than the saturation parameter, only a single real solution of the





intracavity light power exists in resonance. The condition (5) for the onset of on-resonance bistability is represented as dotted black lines in figure 7.

For too strong pumping, as seen in figures 5, the bistability disappears for all values of  $\Gamma$ , and we get spectra resembling that of an empty cavity (ECU for empty cavity-like bistable center phase). The maximum pump rate for which bistability occurs is derived from (50) in the appendix A.5) as,

$$n_\eta \lesssim \frac{N^2 g^2}{8\kappa^2}. \quad (8)$$

which is plotted as continuous black horizontal lines. This upper boundary of the bistable region is met when two out of three solutions become degenerate. The analytically derived phase boundaries agree very well with the simulated phase diagrams.

At pump rates below the limit imposed by (8), the spectra present either on-resonance bistability (NMBC for normal mode bistable center phase), off-resonance bistability (NMBW for normal mode bistable wing phase), both separately (NMBWC for normal mode bistable wing and center phase) or a merging of both bistable spectral regions (ECBC for empty cavity-like bistable center phase), as we will show below. For the onset of off-resonance bistability close to the normal mode splitting resonances Gripp and Orozco [27] derived the condition,

$$n_\eta > \frac{4\sqrt{N}}{3\sqrt{3}} \frac{(\kappa + \Gamma/2)^3}{g\kappa^2}, \quad (9)$$

shown as dash-dotted black lines. We note that for a collective coupling strength comparable to the cavity decay rate, as in our experimental situation and illustrated in figure 6(b), this limit is higher than the critical pump rate according to the condition (8), and thus no off-resonance bistability can occur, which leaves the NMBC bistable phase as the only option. For larger collective coupling strength as shown in figure 6(a), the orange area delimits a NMBW phase where only off-resonance bistability exists (as shown in figure 1(c)), and the green-shaded area delimits a region where both bistabilities coexist in a NMBWC phase; an example of such spectra is also shown in figure 1(h). In the region below both conditions (5) and (9), only a unstable solution exists, which characterizes a normal mode unstable (NMU) phase.

When further increasing the pump rate, the bistable regions of the spectrum merge into a ECBC phase. The lower bound of this region is described by the empirically guessed expression,

$$n_\eta \gtrsim \frac{N(\kappa + 2\Gamma)}{2\kappa}, \quad (10)$$

identified as a dashed black line.

The atomic saturation is an important observable to characterize the different phases of the atom-cavity system. Although more difficult to measure experimentally than the cavity transmission, it gives further insight on the difference between the on-resonance and off-resonance bistability. Figures 7(a) and (b) show

the maximum atomic excited state population achieved when scanning the laser frequency, for the same parameters as for figures 6(a) and (b). We learn from the graphs that, while the presence of off-resonance bistability does not require full saturation of the atomic population [see for example the region in figure 7(a) that corresponds to the orange region in figure 6(a)], it is on the contrary required for the emergence of on-resonance bistability [yellow areas in figures 7(a) and (b) and corresponding areas in figures 6(a) and (b)]. We also note that, while the maximum atomic population is achieved off-resonance for the points below the condition represented by equation (5), it is achieved on-resonance for the points above it, where the full saturation is found. This further confirms that the underlying mechanism for this bistability is the appearance of a transparency window caused by full saturation of the atoms. Moreover, the atomic population presents a discontinuity when going from lower to higher pump rates, as the threshold for the on-resonance bistability is crossed. This is also evident from the two insets of figures 7(a) and (b), calculated for the parameters of [26] and for our experiment, respectively. Since it relies on the full saturation of a quantum two-level transition, the on-resonance bistability cannot stem only from a nonlinear susceptibility and is fully quantum in its origin, at odds with the off-resonance bistability.

### 3.2. Comparison to other experiments

The reason why bistability could be observed in the resonantly coupled regime ( $|\Delta_c| \ll \kappa$ ) in our experiment is that we are deep in the bad-cavity limit. As seen from figure 5, bistability around  $\Delta_c = 0$  appears over wide ranges of pump rates  $\eta_+$  only if  $\Gamma \ll \kappa$ .

Previous experiments [25, 30–32] carried out with alkali atoms were all performed in the good-cavity limit, due to the large spontaneous decay width  $\Gamma$  of the atomic transition. Another experiment carried out by Gothe *et al* [28] employed ytterbium atoms coupled to a cavity via a narrow transition. However, the finesse of the cavity was so high that the atomic decay rate was still twice the cavity decay rate. Consequently, on resonance, spontaneous emission remained the main decay channel. In order to avoid spontaneous emission leading to heating and trap loss they coupled the atoms dispersively to their cavity, so that the bistable features appeared far from the atomic resonance.

## 4. Conclusion

We have observed and characterized a new mechanism for the emergence of saturation-induced bistability in an optical cavity strongly coupled to  $N$  atoms. This new mechanism relies on the complete saturation of a narrow atomic transition quasi-resonant with a cavity mode, where the atomic cloud becomes transparent to the incoming light above a threshold intensity, and a third peak appears in the center between the normal mode resonances. At odds with the previously observed saturation-induced bistability, this new mechanism does not induce an intensity-dependent shift of the frequency for the maximum transmission, and symmetrically induces a bistability window on both sides of the maximum transmission peak. It needs, moreover, a quantum two-level transition to occur, and cannot simply be mimicked by a nonlinear susceptibility in a classical system.

The reason why this new bistability mechanism was just now discovered is that atom-cavity systems are often studied in the good-cavity regime, while this resonant bistability emerges in the bad cavity limit, that is, when  $\Gamma < \kappa$ . In this range of parameters, the coherence of the light-atom interaction is mainly stored within the atomic coherence. This feature has recently received much attention, due to the possibility of using ultra-narrow transitions of strontium atoms coupled to a resonant optical cavity to build ultra-narrow lasers for metrology [10, 13], decoupled from the cavity noise. The proposed regime for achieving ultra-narrow laser emission relies on strong collective coupling between the atoms and the cavity, as well as on the inversion of the atomic population. Thus, bistable effects such as the one reported here are likely to play an important role.

Motivated by the discovery reported here, and in order to provide a complete picture of the whole phase diagram valid in all regimes, we included in our discussion previous experiments performed in the good-cavity limit. We could comprehensively link all phases to the different relevant parameter ratios,  $\Gamma/\kappa$ ,  $\Upsilon_N = N g^2/\Gamma \kappa$ ,  $s_1 = 8 g^2/\Gamma^2$ , and  $n_\eta = s_1 \eta_+$ . This work will guide the exploration of nonlinear coupling between atoms and an optical cavity through up-to-now unexplored regimes, in particular for narrow atomic transitions in the bad cavity limit, where the quantum nature of the atoms cannot anymore be neglected.

The intensity filtering provided by the threshold behavior of the resonant transmission of the cavity can generate non-trivial correlations on the reflected or transmitted light or entanglement between the optical and atomic degrees of freedom. We remember that squeezing has been observed in the light reflected from a ‘bad cavity’ interacting with atoms [20]. Those interesting prospects will be investigated in future work.

## Data availability statement

The data cannot be made publicly available upon publication because they are not available in a format that is sufficiently accessible or reusable by other researchers. The data that support the findings of this study are available upon reasonable request from the authors.

## Acknowledgments

D R acknowledges the Coordenação de Aperfeiçoamento de Pessoal de Nível Superior (CAPES) - Finance Code 001 for scholarships. R C T acknowledges funding from the Brazilian state agency FAPESP, Grant No. 2018/23873-3. Ph W C received support from the project CAPES-COFECUB (Ph879-17/CAPES 88887.130197/2017-01) and FAPESP, Grant No. 2022/00261-8. S S acknowledges funding by the Deutsche Forschungsgemeinschaft (DFG, German Research Foundation) - 422447846 and 465199066, within Research Unit FOR 5413 ‘Long-range interacting quantum spin systems out of equilibrium: Experiment, Theory and Mathematics. We thank Igor Lesanovsky for helpful discussions.

## Appendix. Open Dicke model for atoms distributed over the mode volume of a ring cavity

The starting point for the theoretical description is the open system Dicke Hamiltonian for  $N$  atoms interacting with two counter-propagating modes of an optical ring cavity. The rotating wave approximation having been made, it reads,

$$\hat{H} = \hat{H}_{\text{field}} + \hat{H}_{\text{pump}} + \sum_{j=1}^N \left( \hat{H}_{\text{atom}}^{(j)} + \hat{H}_{\text{atom:field}}^{(j)} \right), \quad (11)$$

with

$$\begin{aligned} \hat{H}_{\text{atom}}^{(j)} &= -\Delta_a \hat{\sigma}_j^+ \hat{\sigma}_j^- = -\frac{\Delta_a}{2} \left( \mathbb{I}_2 + \hat{\sigma}_j^z \right) \\ \hat{H}_{\text{field}} &= -\sum_{\pm} \Delta_c \hat{a}_{\pm}^{\dagger} \hat{a}_{\pm} \\ \hat{H}_{\text{pump}} &= -\sum_{\pm} \eta_{\pm} \left( \hat{a}_{\pm} - \hat{a}_{\pm}^{\dagger} \right) \\ \hat{H}_{\text{atom:field}}^{(j)} &= g \sum_{\pm} \left( \hat{a}_{\pm} \hat{\sigma}_j^+ e^{\pm i k z_j} + \hat{a}_{\pm}^{\dagger} \hat{\sigma}_j^- e^{\mp i k z_j} \right). \end{aligned} \quad (12)$$

Here,  $\Delta_a \equiv \omega - \omega_a$  with  $\omega_a = 2\pi c/\lambda_a$  being the atomic resonance frequency, and  $\Delta_c \equiv \omega - \omega_c$  with  $\omega_c = 2\pi m\delta_{fsr}$  being a cavity resonance frequency.  $\delta_{fsr}$  is the cavity's free spectral range and  $m \in \mathbb{N}$ .  $\eta_{\pm}$  are the pump rates of the two counter-propagating modes,  $g$  the atom-field coupling strength (corresponding to half the single-photon Rabi frequency), and  $g_N = g\sqrt{N}$  is the collective coupling strength.  $\hat{\sigma}_j^+$ ,  $\hat{\sigma}_j^-$ ,  $\hat{\sigma}_j^z$  are the usual Pauli matrices applied to the  $j$ th atom, so that

$$\hat{\mathbf{s}} = \frac{1}{2} \begin{pmatrix} \hat{\sigma}^- + \hat{\sigma}^+ \\ i(\hat{\sigma}^- - \hat{\sigma}^+) \\ [\hat{\sigma}^+, \hat{\sigma}^-] \end{pmatrix} \quad (13)$$

is the atomic spin operator.  $\hat{a}_{\pm}$ ,  $\hat{a}_{\pm}^{\dagger}$  are the usual photonic field operators for the counter-propagating modes.

Note that we do not treat photonic recoil  $e^{\pm i k z_j}$  as a degree of freedom, but just as a parameter depending on the location of the atoms. Decay processes can be considered in a master or in Heisenberg equations via jump operators,  $\hat{L} = \hat{\sigma}^-$ ,  $\hat{a}_{\pm}$ , describing decay processes occurring, respectively, at rates  $\gamma = \Gamma$ ,  $2\kappa$ .

### Derivation of the equations of motion

Using the Hamiltonian (11) and for the decay processes  $\hat{L}$  the Lindblad superoperator expression  $\mathcal{L}_{\gamma, \hat{L}}^{\dagger} \hat{A} = \gamma(2\hat{L}^{\dagger} \hat{A} \hat{L} - \hat{L}^{\dagger} \hat{L} \hat{A} - \hat{A} \hat{L}^{\dagger} \hat{L})$ , we derive the equations of motion for the individual atomic operators,

$$\begin{aligned} \dot{\hat{\sigma}}_i^- &= -i[\hat{\sigma}_i^-, \hat{H}] + \mathcal{L}_{\Gamma/2, \hat{\sigma}_i^-}^{\dagger} \hat{\sigma}_i^- \\ &= (i\Delta_a - \frac{\Gamma}{2}) \hat{\sigma}_i^- + i g (e^{i k z_i} \hat{a}_+ + e^{-i k z_i} \hat{a}_-) \hat{\sigma}_i^z, \end{aligned} \quad (14)$$

and

$$\begin{aligned}\dot{\hat{\sigma}}_i^z &= -\imath [\hat{\sigma}_i^z, \hat{H}] + \mathcal{L}_{\Gamma/2, \hat{\sigma}_i^-}^\dagger \hat{\sigma}_i^z \\ &= -2\imath g (e^{\imath k z_i} \hat{a}_+ + e^{-\imath k z_i} \hat{a}_-) \hat{\sigma}_i^+ \\ &\quad + 2\imath g (e^{-\imath k z_i} \hat{a}_+^\dagger + e^{\imath k z_i} \hat{a}_-^\dagger) \hat{\sigma}_i^- - \Gamma (\mathbb{I}_2 + \hat{\sigma}_i^z)\end{aligned}\quad (15)$$

and for the field operators,

$$\begin{aligned}\dot{\hat{a}}_\pm &= -\imath [\hat{a}_\pm, \hat{H}] + \mathcal{L}_{\kappa, \hat{a}}^\dagger \hat{a}_\pm \\ &= (\imath \Delta_c - \kappa) \hat{a}_\pm - \imath g \sum_j \hat{\sigma}_j^- e^{\mp \imath k z_j} + \eta_\pm.\end{aligned}\quad (16)$$

### Stationary solution

The stationary solution follows from the expectation values of the equations (14)–(16),

$$\begin{aligned}\text{(i)} \quad 0 &= (\imath \Delta_a - \frac{\Gamma}{2}) \langle \hat{\sigma}_i^- \rangle + \imath g (e^{\imath k z_i} \langle \hat{a}_+ \hat{\sigma}_i^z \rangle + e^{-\imath k z_i} \langle \hat{a}_- \hat{\sigma}_i^z \rangle) \\ \text{(ii)} \quad 0 &= -2\imath g (e^{\imath k z_i} \langle \hat{a}_+ \hat{\sigma}_i^+ \rangle + e^{-\imath k z_i} \langle \hat{a}_- \hat{\sigma}_i^+ \rangle) + 2\imath g (e^{-\imath k z_i} \langle \hat{a}_+^\dagger \hat{\sigma}_i^- \rangle + e^{\imath k z_i} \langle \hat{a}_-^\dagger \hat{\sigma}_i^- \rangle) - \Gamma (\mathbb{I}_2 + \langle \hat{\sigma}_i^z \rangle) \\ \text{(iii)} \quad 0 &= (\imath \Delta_c - \kappa) \langle \hat{a}_\pm \rangle - \imath g \sum_j e^{\mp \imath k z_j} \langle \hat{\sigma}_j^- \rangle + \eta_\pm\end{aligned}\quad (17)$$

Neglecting all correlations by setting, e.g.  $\langle \hat{a}_\pm \hat{\sigma}_i^z \rangle = \langle \hat{a}_\pm \rangle \langle \hat{\sigma}_i^z \rangle$ , and analogously for all operator products, we loose phenomena rooted in entanglement, such as spin-squeezing. Using the abbreviations,

$$U_\gamma \equiv U_0 - \imath \gamma_0 \equiv \frac{g^2 (\Delta_a - \frac{\Gamma}{2})}{\Delta_a^2 + \frac{\Gamma^2}{4}} \quad \text{and} \quad \Delta_\kappa \equiv \Delta_c + \imath \kappa, \quad (18)$$

where  $U_0$  has the meaning of a single-photon light shift and  $\gamma_0$  of single-photon scattering rate, equation (17)(i) resolved by  $\langle \hat{\sigma}_i^- \rangle$  becomes,

$$\langle \hat{\sigma}_i^- \rangle = -\frac{U_\gamma}{g} (e^{\imath k z_i} \alpha_+ + e^{-\imath k z_i} \alpha_-) \langle \hat{\sigma}_i^z \rangle. \quad (19)$$

Substituting  $\langle \hat{\sigma}_i^\pm \rangle$  in (17)(ii),

$$\left(1 + 2 \left| \frac{U_\gamma}{g} \right|^2 |e^{\imath k z_i} \alpha_+ + e^{-\imath k z_i} \alpha_-|^2\right) \langle \hat{\sigma}_i^z \rangle = -1, \quad (20)$$

and in (iii),

$$\Delta_\kappa \alpha_\pm + \sum_j U_\gamma (e^{\imath k z_j \mp \imath k z_j} \alpha_+ + e^{-\imath k z_j \mp \imath k z_j} \alpha_-) \langle \hat{\sigma}_j^z \rangle = \eta_\pm. \quad (21)$$

Eliminating  $\langle \hat{\sigma}_j^z \rangle$  from the expressions (20) and (21),

$$\sum_j \frac{-U_\gamma (\alpha_\pm + e^{\mp 2\imath k z_j} \alpha_\mp)}{1 + 2 |U_\gamma/g|^2 |e^{\imath k z_j} \alpha_+ + e^{-\imath k z_j} \alpha_-|^2} = \eta_\pm - \Delta_\kappa \alpha_\pm, \quad (22)$$

which is the expression (2) given in the main text.

### Saturation-induced bistability

It is obvious that the steady-state expression (22) will generate bistable behavior. With the aim of deriving an analytic solution accounting for our experimental situation we assume that the atomic cloud is homogeneously distributed over the cavity's mode volume. The other extreme case that the atoms are perfectly bunched,  $b \equiv \frac{1}{N} \sum_j e^{2\imath k z_j} = 1$ , which is the case when the atoms are arranged in an optical lattice, can be treated analogously and produces similar results except from the fact that the mode  $\alpha_-$  counter-propagating to the pumped mode  $\alpha_+$  may receive a considerable number of photons due to Bragg-enhanced backscattering.

In the case of a homogeneous cloud (no bunching  $b = 0$ ) and with one-sided probing,  $\eta_- = 0$ , we may neglect backscattered light altogether,  $\alpha_- = 0$ . Re-scaling via  $\bar{\Delta}_c \equiv \Delta_c/\kappa$  and  $\bar{\Delta}_a \equiv 2\Delta_a/\Gamma$  and using the definitions of the single-atom cooperativity and the single-photon saturation parameter,

$$\Upsilon \equiv \frac{\Omega_1^2}{\Gamma\kappa} = \frac{4g^2}{\Gamma\kappa} \quad \text{and} \quad s_1 \equiv \frac{2\Omega_1^2}{\Gamma^2} = \frac{8g^2}{\Gamma^2}, \quad (23)$$

the expression (22) simplifies to,

$$\alpha_+ = \frac{\eta_+}{\kappa} \frac{1}{1 - i\bar{\Delta}_c + \frac{N\Upsilon(1+i\bar{\Delta}_a)}{2(1+s_1n+\bar{\Delta}_a^2)}}, \quad (24)$$

so that for the intracavity mean photon number we get,

$$n = \frac{\eta_+^2/\kappa^2}{\left(1 + \frac{N\Upsilon/2}{1+s_1n+\bar{\Delta}_a^2}\right)^2 + \left(\bar{\Delta}_c - \frac{\bar{\Delta}_aN\Upsilon/2}{1+s_1n+\bar{\Delta}_a^2}\right)^2}. \quad (25)$$

The ‘good-cavity’ regime,  $s_1 < \Upsilon$ , and the ‘bad-cavity’ regime,  $s_1 > \Upsilon$ , are delimited by the ratio between the single-photon saturation and the single-atom cooperativity.

The expression (25) can be written in terms of a third order polynomial,

$$0 = An^3 + Bn^2 + Cn + D, \quad (26)$$

with the coefficients,

$$\begin{aligned} A &= s_1^2 (1 + \bar{\Delta}_c^2) \\ B &= 2s_1 \left( \bar{\Delta}_a^2 + \frac{\Upsilon_N}{2} \right) + 2s_1 \bar{\Delta}_c \left[ \bar{\Delta}_c (1 + \bar{\Delta}_a^2) - \frac{N\Upsilon}{2} \bar{\Delta}_a \right] - s_1 s_\eta \\ C &= \left( \bar{\Delta}_a^2 + \frac{\Upsilon_N}{2} \right)^2 + \left[ \bar{\Delta}_c (1 + \bar{\Delta}_a^2) - \frac{N\Upsilon}{2} \bar{\Delta}_a \right]^2 - 2s_\eta (1 + \bar{\Delta}_a^2) \\ D &= -n_\eta (1 + \bar{\Delta}_a^2)^2 \end{aligned} \quad (27)$$

where we defined the collective cooperativity, the maximum photon number, and the maximum saturation parameter,

$$\Upsilon_N \equiv N\Upsilon + 2 \quad \text{and} \quad n_\eta \equiv \frac{\eta_+^2}{\kappa^2} \quad \text{and} \quad s_\eta \equiv s_1 n_\eta. \quad (28)$$

The roots of the cubic equation are given by,

$$R \equiv \sqrt[3]{36CBA - 108DA^2 - 8B^3 + 12\sqrt{3}A\sqrt{4C^3A - C^2B^2 - 18CBAD + 27D^2A^2 + 4DB^3}} \quad (29)$$

and

$$X_\pm \equiv \frac{R}{6A} \pm \frac{6AC - 2B^2}{3AR} \quad (30)$$

so that,

$$n_1 = X_- - \frac{B}{3A}, \quad n_{2,3} = -\frac{1}{2}X_- - \frac{B}{3A} \pm \frac{i\sqrt{3}}{2}X_+, \quad (31)$$

from which we obtain the roots  $n = |\alpha_+|^2$  and the field amplitude from (24).

The atomic state can be obtained from equations (19) and (20),

$$\begin{aligned} \langle \hat{\sigma}_i^z \rangle &= -\frac{1}{1 + 2|U_\gamma/g|^2|\alpha_+ + \alpha_-|^2} \\ \langle \hat{\sigma}_i^- \rangle &= \frac{U_\gamma}{g} (\alpha_+ + \alpha_-) \langle \hat{\sigma}_i^z \rangle. \end{aligned} \quad (32)$$

All numerical curves shown in this work are obtained by evaluating the solutions (31) discarding all solutions with photon numbers  $n \notin \mathbb{R}^+$ . Figures 5 and 8 exhibit spectral ranges characterized by the presence of several solutions, while the theoretical spectra of figures 3(d)–(f) and 4(c) only show the solution corresponding to the highest photon number.



### Critical pump rate on resonance

Let us now discuss the resonant case,  $\Delta_c = 0 = \Delta_a$ , for which equation (24) becomes,

$$\alpha_+ \simeq \frac{\eta_+}{\kappa} \frac{ns_1 + 1}{\frac{1}{2}N\Upsilon + ns_1 + 1} . \quad (33)$$

From this formula we can easily evaluate the relative importance of collective cooperativity and saturation. Since  $N\Upsilon \gg 1$ , we get below saturation,

$$\alpha_+ \xrightarrow{n \rightarrow 0} \frac{\eta_+}{\kappa} \frac{2}{N\Upsilon} , \quad (34)$$

that is, the excitation of the cavity field is heavily suppressed by the normal mode splitting. On the other hand, at high saturation,

$$\alpha_+ \xrightarrow{n \rightarrow \infty} \frac{\eta_+}{\kappa} , \quad (35)$$

the cavity becomes fully transparent.

For intermediate saturation we evaluate the coefficients (27) of the cubic equation (decorated by an apostrophe),

$$\begin{aligned} A' &= s_1^2 \\ B' &= s_1 (\Upsilon_N - s_\eta) \\ C' &= \frac{1}{4}\Upsilon_N^2 - 2s_\eta \\ D' &= -n_\eta . \end{aligned} \quad (36)$$

The cubic equation (26) with the resonant coefficients (36) has three degenerate real solutions if for some coefficient  $n_t$ ,

$$n^3 + \frac{B'}{A'}n^2 + \frac{C'}{A'}n + \frac{D'}{A'} = (n - n_t)^3 . \quad (37)$$

In other words,

$$\frac{B'}{A'} = -3n_t , \quad \frac{C'}{A'} = 3n_t^2 , \quad \frac{D'}{A'} = -n_t^3 . \quad (38)$$

From (38) we derive,

$$\begin{aligned} 3s_1n_t &= s_\eta - \Upsilon_N \\ \frac{3}{4}\Upsilon_N^2 - 6s_\eta &= (s_\eta - \Upsilon_N)^2 \\ 27s_\eta &= (s_\eta - \Upsilon_N)^3 . \end{aligned} \quad (39)$$

The equations are solved for

$$(s_\eta, \Upsilon_N, s_1n_t) = (0, 0, 0), (-1, 2, -3), (27, 18, 3) , \quad (40)$$

the only non-trivial physical solution being the last one. This means, that the onset of bistability occurs when,

$$N\Upsilon = 16 \quad \text{and} \quad n_\eta = 27/s_1 \quad \text{and} \quad n_t = 3/s_1 . \quad (41)$$

The onset is entirely governed by an interplay between the saturation parameter  $s_\eta$ , tuned via the rate at which the cavity is pumped, and the collective cooperativity  $\Upsilon_N$ , which can be controlled via the number of atoms fed into the cavity mode volume. For our experiment this means, that we observe bistability if more than  $N > 1232$  atoms interact with the cavity and the pump rate is high enough to inject  $n_\eta > 2.29$  photons resonantly into the cavity in the absence of atoms. Under these circumstances, we actually find  $n_t > 0.25$  photons in the cavity in the presence of 1232 atoms.

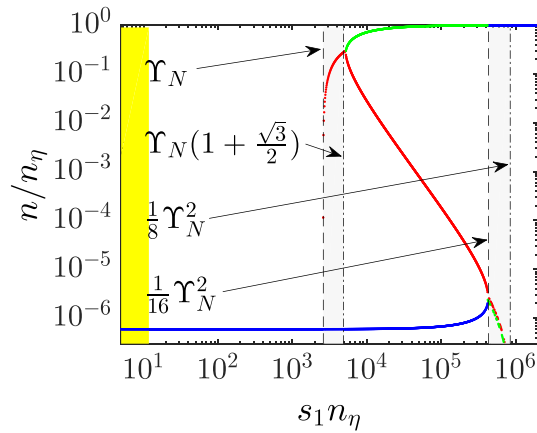


**Figure 8.** Numerical simulations of the normalized intracavity photon number as a function of the normalized pump rate for  $g_N = 1.2\kappa$ . They confirm the existence of a single solution for  $s_1 n_\eta < 2600$  [according to (43)] or for  $s_1 n_\eta > 845\,000$  [according to the right-hand inequality of (46)]. Bistability with three solutions is observed for the interval specified by the left-hand inequality of (46) and by (50), that is,  $4850 < s_1 n_\eta < 432\,000$ . Finally, bistability with two solutions is seen in the remaining intervals. The yellow area marks low saturation.

### Condition for three positive real solutions

The condition  $0 = \frac{d}{dn}(A'n^3 + B'n^2 + C'n + D')$  yields the positions of the turning points of the cubic curve parameterized by (26),

$$n_{\text{turn}} = -\frac{B'}{3A'} \pm \frac{B'}{3A'} \sqrt{1 - \frac{3A'C'}{B'^2}}. \quad (42)$$

In order for the cubic curve to have three (not necessarily degenerate) real roots, the cubic curve must have two distinct maxima. That is, (42) must yield two real solutions (called turning points), which requires  $B'^2 < 3A'C'$ . In order for the cubic curve to have three *positive* real roots, both turning points must be positive. Since  $A' > 0$  we necessarily need  $B' < 0$ , which leads to,

$$\boxed{\Upsilon_N < s_1 n_\eta}. \quad (43)$$

Furthermore, we must satisfy,

$$0 < 1 - \frac{3A'C'}{B'^2} < 1. \quad (44)$$

Inserting the coefficients (36) we obtain,

$$s_\eta^2 - 2\Upsilon_N s_\eta + 6s_\eta + \frac{1}{4}\Upsilon_N^2 > 0 > 6s_\eta - \frac{3}{4}\Upsilon_N^2. \quad (45)$$

For large collective cooperativity,  $\Upsilon_N \gg 1$ , we may simplify,

$$\boxed{\Upsilon_N \left(1 + \frac{\sqrt{3}}{2}\right) < s_1 n_\eta < \frac{\Upsilon_N^2}{8}}. \quad (46)$$

The criterion (46) clarifies, that an essential condition for resonant bistability is a sufficiently large collective cooperativity  $\Upsilon_N \gg 8 + 4\sqrt{3}$ . If this is satisfied, one can always find a pump rate  $\eta_+$  such that bistability can be reached.

The theoretical curve shown in figure 8 shows the photon numbers calculated in resonance,  $\Delta_a = 0 = \Delta_{ca}$  as a function of pump strengths. Bistable phases are recognized by the presence of several solutions marked in different colors. The transitions between different phases are delimited by the conditions (43) and (46) and are marked in figure 8 as vertical black dashed or dash-dotted lines.

In order to derive an analytic expression for the boundary near  $s_1 n_\eta = 432\,000$  (vertical black dashed line in figure 8) we note that the region above the boundary is characterized by the existence of three solutions, two of which are degenerate. These solutions can be found by a procedure similarly to the one previously implemented in equation (37). We plug the coefficients (36) into the ansatz,

$$n^3 + \frac{B'}{A'}n^2 + \frac{C'}{A'}n + \frac{D'}{A'} = (n - n_d)^2(n - n_s) \quad (47)$$

and compare the coefficients. This yields a set of equations in the photon numbers  $n_s$ ,  $n_d$ , and  $n_\eta$ ,

$$\begin{aligned} 0 &= s_1 n_s + 2s_1 n_d + \Upsilon_N - s_1 n_\eta \\ 0 &= 8s_1^2 n_d n_s + 4s_1^2 n_d^2 - \Upsilon_N^2 + 8s_1 n_\eta \\ 0 &= -s_1^3 n_d^2 n_s + s_1 n_\eta. \end{aligned} \quad (48)$$

To find an approximate analytic solution of the set of equations (48), we assume,  $\Upsilon_N \gg 1$  and  $n_s \gg n_d$ , which simplifies the set to,

$$\begin{aligned} 0 &= s_1 n_s - s_1 n_\eta \\ 0 &= 8s_1^2 n_d n_s - \Upsilon_N^2 + 8s_1 n_\eta \\ 0 &= -s_1^3 n_d^2 n_s + s_1 n_\eta. \end{aligned} \quad (49)$$

The solution is,

$$s_1 n_\eta \simeq \frac{\Upsilon_N^2}{16}. \quad (50)$$

### Spectral width of the bistable regime

Here, we want to calculate the spectral width of the bistable regime, that is, the width of the ridge connecting the normal modes of figure 3 and the width of the central feature of figure 4. Unfortunately, the condition  $\Delta_{ca} = \Delta_c - \Delta_a = 0$  entails cumbersome formulas. For simplicity we use instead  $\bar{\Delta}_c = 0$ , which corresponds to a cut along a diagonal emphasized by dotted lines in figure 3. Assuming a small spontaneous decay rate,  $|\bar{\Delta}_a| \gg 1$  and a large collective cooperativity,  $\Upsilon_N \gg 1$ , the coefficients (27) become (decorated by a double apostrophe),

$$\begin{aligned} A'' &= s_1^2 \\ B'' &\simeq s_1 (2\bar{\Delta}_a^2 + \Upsilon_N - s_\eta) \\ C'' &\simeq \bar{\Delta}_a^4 + \left( \frac{\Upsilon_N^2}{4} - 2s_\eta \right) \bar{\Delta}_a^2 \\ D'' &\simeq -n_\eta \bar{\Delta}_a^4. \end{aligned} \quad (51)$$

The coefficient  $B''$  determines the slope of the cubic curve in its turning point. For  $A'' > 0$  it must be negative in order to allow for more than one real solution. Thus, we can use the condition  $B'' = 0$  to deduce that, for small enough spontaneous decay rate, the spectral width of the bistable regime is proportional to the Rabi frequency,

$$|\Delta_a| = \frac{\Gamma}{4} \sqrt{s_\eta - \Upsilon_N} = \frac{1}{2} \sqrt{\frac{\Omega_\eta^2}{2} - \frac{\Gamma^2 \Upsilon_N}{4}} \simeq \frac{\Omega_\eta}{2\sqrt{2}}. \quad (52)$$

### ORCID iDs

R C Teixeira  <https://orcid.org/0000-0001-8358-861X>

S Slama  <https://orcid.org/0000-0001-8993-7657>

### References

- [1] Kitagawa M and Ueda M 1993 Squeezed spin states *Phys. Rev. A* **47** 5138
- [2] Leroux I D, Schleier-Smith M H and Vuletic V 2010 Implementation of cavity squeezing of a collective atomic spin *Phys. Rev. Lett.* **104** 073602
- [3] Schleier-Smith M H, Leroux I D and Vuletic V 2010 Squeezing the collective spin of a dilute atomic ensemble by cavity feedback *Phys. Rev. A* **81** 021804(R)
- [4] Schleier-Smith M H, Leroux I D and Vuletic V 2010 States of an ensemble of two-level atoms with reduced quantum uncertainty *Phys. Rev. Lett.* **104** 073604
- [5] Chen Z, Bohnet J G, Sankar S R, Dai J and Thompson J K 2011 Conditional spin squeezing of a large ensemble via the vacuum Rabi splitting *Phys. Rev. Lett.* **106** 133601
- [6] Bohnet J G, Cox K C, Norcia M A, Weiner J M, Chen Z and Thompson J K 2014 Reduced spin measurement back-action for a phase sensitivity ten times beyond the standard quantum limit *Nat. Photon.* **8** 731
- [7] Cox K C, Greve G P, Weiner J M and Thompson J K 2016 Deterministic squeezed states with collective measurements and feedback *Phys. Rev. Lett.* **116** 093602
- [8] Xu M, Jäger S B, Schütz S, Cooper J, Morigi G and Holland M J 2016 Supercooling of atoms in an optical resonator *Phys. Rev. Lett.* **116** 153002

- [9] Salvi L, Poli N, Vuletić V and Tino G M 2018 Squeezing on momentum states for atom interferometry *Phys. Rev. Lett.* **120** 033601
- [10] Meiser D, Ye J, Carlson D R and Holland M J 2009 Prospects for a milliHertz-linewidth laser *Phys. Rev. Lett.* **102** 163601
- [11] Maier T, Kraemer S, Ostermann L and Ritsch H 2014 A superradiant clock laser on a magic wavelength optical lattice *Opt. Exp.* **22** 13269
- [12] Norcia M A, Winchester M N, Cline J R K and Thompson J K 2016 Superradiance on the milliHertz linewidth strontium clock transition *Sci. Adv.* **2** e1601231
- [13] Norcia M A and Thompson J K 2016 Cold-strontium laser in the superradiant crossover regime *Phys. Rev. X* **6** 011025
- [14] Norcia M A, Lewis-Swan R J, Cline J R K, Zhu B, Rey A M and Thompson J K 2018 Cavity-mediated collective spin-exchange interactions in a strontium superradiant laser *Science* **361** 259
- [15] Davis E J, Bentsen G, Homeier L, Li T and Schleier-Smith M H 2019 Photon-mediated spin-exchange dynamics of spin-1 atoms *Phys. Rev. Lett.* **122** 010405
- [16] Bychek A, Hotter C, Plankensteiner D and Ritsch H 2021 Superradiant lasing in inhomogeneously broadened ensembles with spatially varying coupling (arXiv:2105.11023)
- [17] Orioli A P, Thompson J K and Rey A M 2022 Emergent dark states from superradiant dynamics in multilevel atoms in a cavity *Phys. Rev. X* **12** 011054
- [18] Hosten O, Krishnakumarn R, Engelsen N J and Kasevich M A 2016 Quantum phase magnification *Science* **352** 1552
- [19] Cline J R K, Schafer V M, Niu Z, Young D J, Hyun Yoon T and Thompson J K 2022 Continuous collective strong coupling between atoms and a high finesse optical cavity (arXiv:2211.00158v1)
- [20] Lambrecht A, Coudreau T, Steinberg A M and Giacobino E 1996 Squeezing with cold atoms *Europhys. Lett.* **36** 93
- [21] Turchette Q A, Georgiades N P, Hood C J, Kimble H J and Parkins A S 1998 Squeezed excitation in cavity QED: experiment and theory *Phys. Rev. A* **58** 4056
- [22] Schnabel R, Mavalvala N, McClelland D E and Lam P K 2016 Quantum metrology for gravitational wave astronomy *Nat. Commun.* **7** 121
- [23] Louchet-Chauvet A, Appel J, Renema J, Oblak D, Kjaergaard N and Polzik E S 2009 Entanglement-assisted atomic clock beyond the projection noise limit *New J. Phys.* **12** 065032
- [24] Dantan A, Cviklinski J, Giacobino E and Pinard M 2006 Spin squeezing and light entanglement in coherent population trapping *Phys. Rev. Lett.* **97** 023605
- [25] Gibbs H M, McCall S L and Venkatesan T N C 1976 Differential gain and bistability using a sodium-filled Fabry-Pérot interferometer *Phys. Rev. Lett.* **36** 1135
- [26] Gripp J, Mielke S L and Orozco L A 1997 Evolution of the vacuum Rabi peaks in a detuned atom-cavity system *Phys. Rev. A* **56** 3262
- [27] Gripp J and Orozco L A 1997 Evolution of the vacuum Rabi peaks in a many-atom system *Quantum Semiclass. Opt.* **8** 823
- [28] Gothe H, Valenzuela T, Cristiani M and Eschner J 2019 Optical bistability and nonlinear dynamics by saturation of cold Yb atoms in a cavity *Phys. Rev. A* **99** 013849
- [29] Martin M J, Meiser D, Thomsen J W, Ye J and Holland M J 2011 Extreme nonlinear response of ultranarrow optical transitions in cavity QED for laser stabilization *Phys. Rev. A* **94** 063813
- [30] Gupta S, Moore K L, Murch K W and Stamper-Kurn D M 2007 Cavity nonlinear optics at low photon numbers from collective atomic motion *Phys. Rev. Lett.* **99** 213601
- [31] Ritter S, Brennecke F, Baumann K, Donner T, Guerlin C and Esslinger T 2009 Dynamical coupling between a Bose-Einstein condensate and a cavity optical lattice *Appl. Phys. B* **95** 213
- [32] Lambrecht A, Courty J and Giacobino E 1995 Optical nonlinear dynamics with cold atoms in a cavity *Opt. Commun.* **115** 199
- [33] Gabor B, Nagy D, Dombi A, Clark T W, Williams F I B, Adwaith K V, Vukics A and Domokos P 2022 Ground state bistability of cold atoms in a cavity *Phys. Rev. A* **107** 023713
- [34] Suarez E, Carollo F, Lesanovsky I, Olmos-Sanchez B, Courteille P W and Slama S 2023 Collective atom-cavity coupling and nonlinear dynamics with atoms with multilevel ground states *Phys. Rev. A* **107** 023714
- [35] Zhu Y, Gauthier D J, Morin S E, Wu Q, Carmichael H J and Mossberg T W 1990 Vacuum Rabi splitting as a feature of linear-dispersion theory: analysis and experimental observations *J. Opt. Soc. Am. B* **64** 2499
- [36] Schuster I, Kubanek A, Fuhrmanek A, Puppe T, Pinske P W H, Murr K and Rempe G 2001 Nonlinear spectroscopy of photons bound to one atom *Nat. Phys. Lett.* **4** 382
- [37] Mücke M, Figueroa E, Bochmann J, Hahn C, Murr K, Ritter S, Villas-Boas C J and Rempe G 2010 Electromagnetically induced transparency with single atoms in a cavity *Nature* **465** 755
- [38] Arnold K J, Baden M P and Barrett M D 2011 Collective cavity quantum electrodynamics with multiple atomic levels *Phys. Rev. A* **84** 033843
- [39] Ritsch H, Domokos P, Brennecke F and Esslinger T 2013 Cold atoms in cavity-generated dynamical optical potentials *Rev. Mod. Phys.* **85** 553
- [40] Rivero D, Beli Silva C, Moreno Armijo M A, Keßler H, da Silva H F, Comito G, Shiozaki R F, Teixeira R C and Courteille P W 2021 Progress towards a continuously operating matter wave interferometer for inertial sensing *Appl. Phys. B* **128** 44
- [41] Note that the decrease of the normal mode splitting at high intensities seen in various figures [e.g. black lines in figures 4(c) and 5(b)] is a consequence of the nonlinearity of the system even in regimes where no bistability is observed
- [42] Narducci L M, Orzag M and Tuft R A 1973 Energy spectrum of the Dicke Hamiltonian *Phys. Rev. A* **8** 1892
- [43] Garraway B M 2011 The Dicke model in quantum optics: Dicke model revisited *Phil. Trans. R. Soc. A* **369** 1137
- [44] Note that all features observed with a ring cavity in this work also apply to linear cavities
- [45] Landau L D and Lifschitz E M 1976 Small oscillations *Mechanics* 3rd edn, ed L D Landau and E M Lifschitz (Butterworth-Heinemann) ch V, pp 58–95
- [46] Winchester M N, Norcia M A, Cline J R K and Thompson J K 2017 Magnetically induced optical transparency on a forbidden transition in strontium for cavity-enhanced spectroscopy *Phys. Rev. Lett.* **118** 263601